Observing what cannot be observed: computational electrochemistry from carbon to hydrogen

Hanselman, S.R.

> Chapter 1

Introduction

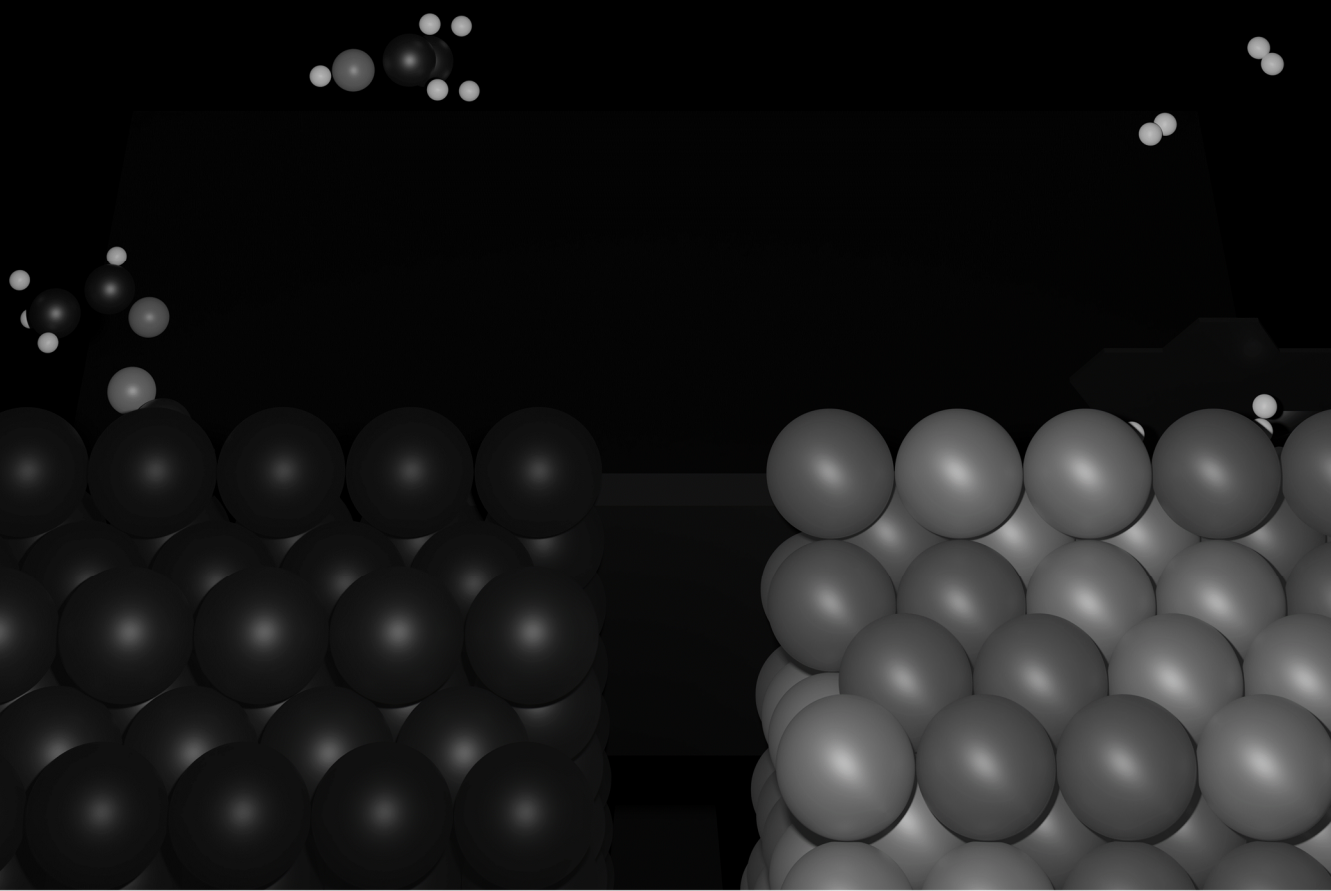

1.1. General introduction: Electrocatalysis for the environment

Our current patterns of energy consumption and production are unsustainable from both a resource and an environmental perspective. In fact, the Intergovernmental Panel on Climate Change (IPCC) predicts a rise in global temperatures of over 2 °C if we do not radically depart from using fossil fuels.[1] Even a temperature rise limited to 1.5 °C would have a significant impact on nature and human life in many parts of the world.[2] Moreover, fossil resources are depleted faster than they are regenerated,[3,4] even considering that entirely depleting them may in any scenario be incompatible with limiting further global heating below 1.5 °C.[5] As part of an effort to abate these crises, the Paris agreement was signed by 195 UN member states as of the moment of writing (2022).[6] This agreement calls for all nations to limit greenhouse gas emissions:[7] reducing, replacing, and even capturing emissions of (i.e. reusing) fossil fuels is considered of the greatest importance.[7,8] Renewable energy, of which wind and solar energy do not require specific geological features to function, are the prime candidates for replacing fossil fuels. However, both wind and solar energy supplies are either variable or even intermittent,[9–12] hence requiring energy storage to be sufficiently stable for full replacement.[11,13–15] Moreover, renewable energy itself cannot replace fossil-based materials directly, since these are not only used as a source of energy, but also as synthetic feedstocks or industrial fuels.[16] Replacing these fuels and feedstocks therefore requires synthesis from non-fossil resources using renewable energy. Electrochemistry – more specifically, electrocatalysis – is key to solving both issues.[13–16]

In electrolytic cells, an externally applied electric potential difference across two electrodes is used for the oxidation and reduction of chemical species. In galvanic cells, the electromotive force of redox processes is in turn used to produce electricity. These two types of electrochemical systems allow us to store energy in or retrieve energy from active chemical species in a highly controlled fashion. Electrocatalysis is electrochemistry applied to the acceleration of chemical reactions: applied potentials are used to stabilise otherwise thermodynamically unfavourable intermediates, thereby facilitating the selective formation of specific reduction or oxidation products. Such processes are generally less thermochemically demanding than conventional heterogenous catalysis processes. Two forms of electrocatalysis exist, following the respective definitions by Zhang *et al.*:[17] homogeneous electrocatalysis, in which oxidation state of the catalyst is changed using an electrode to oxidise or reduce a target molecule in solution;[18] and heterogeneous electrocatalysis, in which the electrode itself contains the catalytically active sites.[19] In this thesis, we will focus on heterogeneous electrocatalysis.

Research in heterogeneous electrocatalysis focuses on three main aspects: characterisation of the (chemical) structure of the electrocatalytic active sites, description of reaction mechanisms, and definition and optimisation of electrocatalytic activities. The goal is to use the knowledge about these aspects of an electrocatalyst, or several different electrocatalysts, to optimise the chemical composition and other underlying physical parameters; thereby one may increase the yield of, and improve selectivity towards the

desired reaction products.[20,21] Various analysis techniques are used to obtain more information on the nature of an electrocatalytic process. Apart from the conventional analysis of reaction products, cyclic voltammetry (CV) is used to find the onset potential and elucidate the kinetics of specific redox reactions,[22] infrared (IR) spectroscopy helps to characterise on-surface adsorbates and their binding properties,[23] and *operando* X-ray spectroscopy to find the structure of the active surface,[24] among others. Although these methods provide a great source of information on the nature and function of catalytic materials, for most reactions they do not provide all the information needed to describe and optimise the catalytic process. Specifically, short-lived or bottleneck intermediates are key to optimising catalysis. These intermediates are hard to detect relative to less important, yet more abundant adsorbates, especially on suboptimal electrocatalysts. The structure of a surface during the catalytic reaction may also be hard to elucidate *in operando*. If we want to ascertain the structure and composition of the catalyst surface during operation, the identity of important catalytic intermediates, and the underlying relations binding the two, we need to use computational chemistry.[21]

1.2. Computational chemistry

Computational chemistry is the study of molecular systems and chemical reactions using computer simulations. Depending on the chemical system one wishes to describe, simulations can include macroscopic continuum calculations such as fluid or solid mechanics, or microscopic or atomistic simulations in which the focus lies on individual molecules and atoms or small ensembles thereof.[25] In the latter category, two types of simulations can be discerned: molecular mechanics, which uses classical mechanics to simulate atomic interactions using bonding models and force-field methods,[26,27] and quantum chemical calculations; these may be combined in the form of QM/MM simulations.[28,29] Quantum chemical calculations, also called *ab-initio* simulations,[27,30] provide a more accurate description of the electronic structure and distribution of electrons in chemical systems,[30,31] which is of prime importance when describing the molecule-solid interactions fundamental to heterogeneous electrocatalysis. Density functional theory – used in the work presented in this thesis – is arguably the most widely applicable and used method within the scope of ab-initio simulations.[31]

1.2.1. The wavefunction interpretation and its limitations

Along with the wavefunction interpretation, in which wavefunctions behave as described by the Schrödinger equation, density functional theory (DFT) is one of the key approaches to approximating the Schrödinger equation. In the wavefunction interpretation of quantum mechanics, the properties or states of individual particles ($n = 1$) or collections of n particles are described using wavefunctions $\Psi(\vec{r}_1, \dots, \vec{r}_n, t)$ or $|\Psi>$, where $\vec{r}_i$ are the spatial coordinates of particle i. For these wavefunctions, the probability of finding the entire set of particles in specific sites $\{\vec{r}_1, \dots, \vec{r}_n\}$ is equal to $\Psi^*(\vec{r}_1, \dots, \vec{r}_n)\Psi(\vec{r}_1, \dots, \vec{r}_n)$, of which the integral for all coordinates combined over space $<\Psi|\Psi>$ is equal to 1 where $<\Psi|$

represents the complex conjugate of the wavefunction. Similarly, the value of an observable X for a system – including energy and momentum – is defined as $< \Psi|\hat{X}|\Psi >$, where $\hat{X}$ is the corresponding quantum operator. The time dependency of the wavefunction is described using the *time-dependent Schrödinger equation*, which contains the Hamiltonian operator ($\hat{H}$), a specific quantum operator that describes the energy of the system for a specific combination of $\vec{r}$:

$$i\hbar\frac{\partial}{\partial t}\Psi(\vec{r}_1,\dots,\vec{r}_n,t) = \hat{H}\Psi(\vec{r}_1,\dots,\vec{r}_n,t) \quad (1)$$

where $\hbar$ is the reduced Planck constant and the Hamiltonian operator $\hat{H}$ representing the total energy is defined as the sum of the kinetic energy ($\hat{T}$) and potential energy ($\hat{V}$) operators:

$$\hat{H} = \hat{T} + \hat{V} = \sum_{i=1}^{n}\frac{-\hbar^2}{2m_i}\nabla_{\vec{r}_i}^2 + V(\vec{r}_1,\dots,\vec{r}_n,t) \quad (2)$$

where m_i is the mass of particle *i*. Any wavefunction can be expressed as a linear combination of stable wavefunctions or eigenfunctions of the Hamiltonian, as described in the *time-independent Schrödinger equation*:

$$\hat{H}\Psi(\vec{r}_1,\dots,\vec{r}_n,t) = E\Psi(\vec{r}_1,\dots,\vec{r}_n,t) \quad (3)$$

These eigenfunctions do not have any net momentum, nor do they show any change in density with time, and depend on time only with a phase factor $\exp\left(-\frac{i(Et+\phi)}{\hbar}\right)$ where ϕ can be any real number. Note that any wavefunction that is stable for many particles, must be stable for every single particle described by the wavefunction. Hence, in order to calculate the all-electron wavefunction representing the entire system, we can express it in terms of the single particle, non-interacting wavefunctions which are solutions to the single non-interacting particle Schrödinger equation as an initial guess:

$$\hat{H}\psi(\vec{r}) = \frac{-\hbar^2}{2m}\nabla^2 + V_{bg}(\vec{r}) = E\psi(\vec{r}) \quad (4)$$

where $V_{bg}(\vec{r})$ is the background potential experienced by the single non-interacting particle. Its solutions are orthonormal, and hence neither show net overlap in spatial distribution, nor in spin or any other relevant quantum property. This obviously does not take into account particle-particle interactions, which means we can only describe the entire system if we take all possible distributions of the individual particle into account. Before adding the interaction energies, we must consider that some of the particles are identical, and hence are indistinguishable while sharing the set of available single-particle wavefunctions: switching two atomic positions should either yield the same wavefunction if the atoms are allowed to be in the same wavefunction (bosonic particles), or yield the wavefunction multiplied by –1 if atoms are not allowed to be in the same wavefunction (fermionic particles). For bosons, having two equal wavefunctions for two particles keeps the wavefunction a valid solution of the Schrödinger equation; for fermions, it annihilates the entire wavefunction which means multiple particles cannot coexist in the same state. For fermions, the necessary anti-symmetry is ensured by defining the wavefunction Ψ_i as a sum over products of single-particle wavefunctions that obeys the above conditions for the

non-interacting system, which are called Slater determinants.[32] Hence for the identical particles in the wavefunction:

$$\Psi_i(\vec{r}_1, \dots, \vec{r}_n, t) = \sum_{\{j\}_i \subset C_{ni}} \frac{1}{\sqrt{N!}} (\psi_{j,1}(\vec{r}_1)\psi_{j,2}(\vec{r}_2) \dots \psi_{j,N}(\vec{r}_N) - \psi_{j,1}(\vec{r}_2)\psi_{j,2}(\vec{r}_1) \dots \psi_{j,N}(\vec{r}_N) + \cdots) \quad (5)$$

Since we have split the wavefunction into terms which are products of the individual non-interacting particle wavefunctions, we can now further separate the energy terms in the Hamiltonian:

$$\hat{H}\Psi = \sum_{i=1}^{n} \left(\frac{-\hbar^2}{2m_i} \nabla_{\vec{r}_i}^2 + V_{bg}(\vec{r}_i) + \sum_{j \neq i} V_{ij}(\vec{r}_j - \vec{r}_i) \right) \Psi = E\Psi \quad (6)$$

The total wavefunction is expressed as a linear combination of Slater determinants, and c_i can be optimised to obtain the true ground and excited states of the multi-particle wavefunction. However, the resulting equation is analytically unsolvable and very hard to solve numerically due to the N^2 interactions between particles, which all need to be calculated during each computational iteration. It would, therefore, be preferable to avoid the usage of single particles and calculate the entire system of many particles at once.

1.2.2. Basics of density functional theory

Density functional theory is based on the aforementioned principle that if particles are indistinguishable, only the overall density can be observed, which depends directly on the wavefunctions of the N individual particles:[31]

$$\rho(\vec{r}) = \sum_{i=0}^{N} \rho_i(\vec{r}; \psi_0, \dots, \psi_N) \quad (7)$$

It may appear that the density does not describe the particles completely, since the complex part of the wavefunction is obscured by the multiplication with the complex conjugate above. However, any complex prefactor has no physical meaning: since the probability distribution of individual wavefunctions depends on their own unique Hamiltonians, and the effect of the potential energy on the wavefunction only depends on this probability distribution, the density itself is coupled one-on-one to the underlying potential energy.[33] This is the first Hohenberg-Kohn theorem.[33] Now we can redefine the above Hamiltonian in terms of the density at specific locations, expressed in density functionals corresponding to the various energy contributions to the system:[33]

$$E[\rho(\vec{r})] = T[\rho(\vec{r})] + V_{bg}(\vec{r})\rho(\vec{r}) + \iiint_V V_{cl}(\vec{r}_1 - \vec{r})\rho(\vec{r}_1)\rho(\vec{r})d\vec{r}_1 + \iiint_V V_{xc}[\rho(\vec{r}_1); \rho(\vec{r})]d\vec{r}_1 \quad (8)$$

In this equation, T is the kinetic energy, V_{bg} is the background potential or potential generated by non-identical particles, and V_{cl} is the classical interaction within the charge density distribution. Note that these three terms only describe classical interactions; V_{xc} is the exchange-correlation functional which takes into account local energy deviations from the classical energy caused by quantum statistical deviations of particle-particle interactions in a many-particle system. More simply put, even though the probability density for each particle may be high in one position if one ignores interactions, it is highly unlikely that they are close together when observed together if their interactions are repulsive, and that they are far apart if their interactions are attractive. The exchange-correlation functional, and the kinetic energy functional, are non-trivial.

The kinetic energy is defined for each separate particle, as can be deduced from Eqs. 2 and 6. In turn, Eq. 7 – as noted by Hohenberg and Kohn themselves, in their application of the Thomas-Fermi model for electron gases –[33] shows that we can separate the total density into densities ρ_i for individual particles. This principle was used by Kohn and Sham to define hypothetical complex wavefunctions φ_i for each individual particle: the Kohn-Sham wavefunctions.[34] Applying the Schrödinger equation to the kinetic part of the equation, and adapting the potential energy part from Eq. 8, yields the Kohn-Sham equations for the system:

$$\frac{-\hbar^2}{2m}\nabla^2\varphi_i(\vec{r}) + V_{bg}(\vec{r})\varphi_i(\vec{r}) + \varphi_i(\vec{r})\iiint_V V_{cl}(\vec{r}_1 - \vec{r})\rho(\vec{r}_1)d\vec{r}_1 + \frac{\delta V_{xc}[\rho(\vec{r})]}{\delta\rho(\vec{r})}\varphi_i(\vec{r}) = \epsilon_i\varphi_i(\vec{r}) \quad (9)$$

In these equations, the kinetic energy is calculated explicitly. According to the second Hohenberg-Kohn theorem, optimising these systems of equations, and deriving the overall density $\rho(\vec{r})$ from the optimized $\varphi_i(\vec{r})$, gives us the overall energy of the system when we insert $\rho(\vec{r})$ into Eq. 8. However, one unknown quantity remains: the exchange-correlation functional. A perfect (or universal) density functional would include all possible non-classical interactions exactly, whether near or far. Unfortunately, this would require knowledge of particle densities and their interactions for all possible $\vec{r}$. A perfect density functional calculation would hence be equally (in)feasible as a perfect wavefunction calculation.[35]

Therefore, we must approximate the exchange-correlation functional, such that calculations of all interactions or properties of the systems we need are sufficiently accurate, or at least the trends between them are. There are multiple types of practically usable exchange-correlation functionals,[36] which include those based on local densities $\rho(\vec{r})$ (local density approximation functionals or LDAs), density gradients $\nabla\rho(\vec{r})$ in generalized gradient approximation (GGA) functionals, such as the Perdew-Burke-Ernzerhof (PBE) functional,[37] up to non-local functionals which take into account long-range interactions, such as the various Van der Waals (vdW) functionals,[38] and hybrid functionals containing exact exchange.[39,40] The way the functional depends on (derivatives of) densities

can be defined using either model quantum systems – non-empirical functionals – or through analysis of previously calculated and experimental datasets – semi-empirical functionals.[41] Although semi-empirical functionals are usually more accurate for systems similar to those used to obtain the functional, non-empirical functionals remain closer to the underlying physics, bear a lower risk of overfitting and hence overspecialising, and are in that respect more general.[41] The choice of exchange-correlation functional is important; one must verify the applicability of individual functionals to a new system if the desired results are known, and observe whether calculations are consistent across different functionals if the desired results are unknown.[35,41–44]

Apart from the density functional, in practice we need to apply several other approximations to successfully and efficiently perform a DFT calculation. Firstly, we generally assume that wavefunctions of atomic nuclei and electrons are only coupled through their classical interactions.[45] This enables the nuclei to be described separately, usually as point particles. A practical approximation for any computer that is not a perfect Turing machine is the wavefunction cut-off: since memory is limited, we are forced to set a cut-off beyond which we cannot see finer detail. For DFT implementations with periodic-boundary conditions, as the one used in the work presented in this thesis, this is generally described as if it were a free particle energy, with greater energies representing shorter wavelengths and hence finer detail. Another approximation – using pseudopotentials – serves to reconcile the wavefunction cut-off described above with the necessity of fine detail and strong density gradients near nuclei. These pseudopotentials combine the nuclei with core electrons into a set of potentials and densities which may even be perturbed by the surrounding electrons.[46,47] Thereby, fewer electrons need to be taken into account in the DFT calculations, less detail is needed close to the nuclei, and yet we still obtain similarly accurate energies and density distributions. Finally, some calculations with wavefunction energies close to the Fermi level are highly unstable under normal circumstances due to optimisation of wavefunctions affecting which Kohn-Sham wavefunctions are occupied. For these calculations, part of the electronic density just below the Fermi level is redistributed to the wavefunctions just above the Fermi level; this procedure is called smearing, and can be corrected for numerically after energy optimisation.[48] Finally, the Brillouin zone for continuous systems is approximated using *k*-points, which will be discussed in the next section.

1.2.3. Thermodynamics of molecular systems

With all the caveats and methods discussed above, DFT allows us to calculate the internal energies and other system properties needed to approximate the overall free energy of the system; this free energy represents the overall probability of finding one configuration of atoms, or rather a *set of* configurations which are deemed equivalent or related based on our chemical definitions. If we define the temperature, and thereby a weighted average energy for all different configurations combined, as being constant, we find for reasons extensively described by Gibbs,[49] that for independent particles the Boltzmann distribution

applies. In this distribution, the probability P_i depends on particle energy E_i, Boltzmann constant k_B and temperature T as follows:

$$P_i \propto \exp\left(\frac{-E_i}{k_B T}\right) \tag{10}$$

For fermionic particles or states, which are identical and cannot coexist in the same state, the Fermi-Dirac distribution applies:[50,51]

$$P_i \propto \frac{1}{1 + exp\left(\frac{E_i - \mu}{k_B T}\right)} \tag{11}$$

Besides, for bosonic particles or states, which are identical yet may coexist in the same state, the Bose-Einstein distribution applies:[52]

$$P_i \propto \frac{1}{exp\left(\frac{E_i - \mu}{k_B T}\right) - 1} \tag{12}$$

The total probability of any set of configurations is the sum over all probabilities for all configurations $P = \sum_i P_i$, which is called the partition function Z. If we invert Eq. 10 for this cumulative probability, the resulting energy is the (Helmholtz) free energy of the system:

$$F = -k_B T\, ln(Z) = -k_B T\, ln\left(\sum_i P_i\right) \tag{13}$$

It is more common to use the Gibbs free energy for a system in chemistry:

$$G = F + pV \tag{14}$$

This free energy is analogous to the Helmholtz free energy yet assumes the pressure on the system is constant as opposed to the volume of the system. However, the pressure in electrochemical systems is usually no greater than 1 bar, while overall volume changes during an electrochemical reaction are generally small enough for us to safely ignore pV. As a practical impression of the volume change necessary, a change in volume of 1.6×10^5 Å^3, which would be chemically significant (~0.01 eV), would correspond to a cube with each dimension 25 hydrogen-hydrogen distances long, which is larger than almost all reactions caused by a single atom. Thus, in practice, $G \approx F$. The Helmholtz energy, and thereby the Gibbs energy, is separated into internal energy and entropy terms:

$$G \approx F = E - TS \tag{15}$$

Here the internal energy is the weighted sum over all individual state energies,

$$E = \sum_i \frac{P_i E_i}{Z} = \frac{-1}{Z} \frac{\partial Z}{\partial\left(\frac{1}{k_B T}\right)} \tag{16}$$

and the entropy captures the non-internal energy part of the free energy, rather dependent on the availability of different states to each particle:

$$S = \frac{-F + E}{T} = k_B\, ln(Z) - \frac{1}{TZ} \frac{\partial Z}{\partial\left(\frac{1}{k_B T}\right)} \tag{17}$$

If we want to calculate the thermodynamic quantities listed above for the adsorbate systems we are interested in, we must first define which domains of atomic coordinates we consider chemically equivalent. For molecular systems, these atomic coordinates centre around local optima of the atomic positions: here, the potential energy surface is at a minimum, and no net force is exerted by the electrons or any applied electric field on the nuclei. Additionally, the domains of atomic coordinates span across all combinations of atomic positions which eventually converge to the local optimum, when allowed to move along their respective forces imposed by the potential energy surface.

Within these domains of atomic coordinates, one can find nuclear and electronic wavefunctions for which the Hamiltonian is constant for all relevant atomic coordinates and hence are stable. These wavefunctions are the translational and rovibrational modes of the system. For most intents and purposes these modes are split into translational modes, in which the centre of mass moves in space, rotational modes, in which rotational modes involve all-atom motion considered independent of potential energy; and vibrational modes, in which atomic motion is significantly impeded by the potential energy surface. This means we can split the free energy of the system into three terms, with each having their own internal energy and entropy components:

$$G = G_{el} + G_{vib} + G_{rot} + G_{tr} = E_{el} + E_{vib} + E_{rot} + E_{tr} - (TS_{el} + TS_{vib} + TS_{rot} + TS_{tr}) \quad (18)$$

1.2.4. DFT and atomistic thermodynamics

The electronic energy E_{el} for a configuration is obtained by first picking an initial candidate atomic configuration, and subsequently relaxing all relevant atoms to a local optimum. During relaxation, the electronic densities are optimised first using DFT as described above. Subsequently, the forces exerted by the electronic density and any applied field on the atomic nuclei are calculated. If the resulting forces are above the atomic force threshold, the nuclei are moved according to the forces exerted on them. They may move towards any nearby local optimum depending on the aggressivity of the relaxation algorithm. If the atomic forces are below the threshold, the resulting configuration has converged, and the corresponding DFT energy E_{DFT} is equivalent to E_{el} for free molecules or adsorbates, with an offset depending on the choice of functional or computational method. Molecular-molecular contributions have to be accounted for externally, either by calculating the interactions between molecules in a crystalline lattice, or by adding phase-change enthalpies ΔG_{phase} from the gas phase to the liquid or solid phase. S_{el} is usually ignored, since it is negligible for materials with a band gap greater than $k_B T$ and is not very dependent on surface-adsorbate interactions for conductors, since the conducting bands themselves are based on large numbers of atoms and are only slightly perturbed by an adsorbate.

Vibrational thermodynamics

Calculating the vibrational energy E_{vib} and entropy S_{vib} requires modelling the potential energy landscape near the local optimum and obtaining the vibrational modes with their respective free energies. A first approximation of the potential energy surface near the local optimum is that the potential energy is quadratic in all directions:

$$V_{harm}(\vec{r}) = E_{el} + \left(\vec{r} - \vec{r}_{opt}\right)^T \boldsymbol{V} \left(\vec{r} - \vec{r}_{opt}\right) \tag{19}$$

The forces on the atoms are:

$$\vec{F}(\vec{r}) = -\nabla V_{harm}(\vec{r}) = -2\boldsymbol{V}\left(\vec{r} - \vec{r}_{opt}\right) = \boldsymbol{F}\left(\vec{r} - \vec{r}_{opt}\right) \tag{20}$$

Matrix $\boldsymbol{F}$, which consists of elements $F_{i,j}$, consists of the individual forces per unit distance on atomic coordinate j exerted by a displacement in atomic coordinate i. This matrix can be approximated using the *single-atom displacement* method.[53] In this method, one or multiple displacements of a single atom are taken along each relevant atomic coordinate, forces per unit distance are calculated for each displacement, and a (weighted) average force per unit distance is calculated from these values for each atomic coordinate. The corresponding accelerations, defining the dynamic matrix of the atoms, are:

$$\vec{a}(\vec{r}) = \boldsymbol{D}\left(\vec{r} - \vec{r}_{opt}\right) \tag{21}$$

where, since $\vec{a} = \frac{\vec{F}}{m}$, the dynamic matrix $\boldsymbol{D}$ depends on the square root of the masses of atoms involved:[53]

$$D_{i,j} = \frac{F_{i,j}}{\sqrt{m_i m_j}} \tag{22}$$

Stable vibrational modes are those in which accelerations are parallel to displacements: these correspond to the eigenvectors of matrix $\boldsymbol{D}$, or $\vec{r}_i$. The corresponding eigenvalues d_i are equal to the square of the vibrational frequencies, and when these are inserted into the equations for the quantum harmonic oscillator, the energies of the various vibrational modes of the oscillator are for any integer n:

$$E_n = \left(n + \frac{1}{2}\right)\hbar\sqrt{d_i} = \left(n + \frac{1}{2}\right)E_{exc} \tag{23}$$

where E_{exc} is the excitation energy of the quantum harmonic oscillator. The minimum or zero-point energy of the oscillator is $E_{ZPE} = \frac{1}{2}E_{exc}$.[53,54]

All vibrational modes in the harmonic oscillator model are independent and can be linearly combined, which means each mode has its own internal energy and entropy. Moreover, each vibrational mode can be excited n times, and one mode cannot be excited to different n simultaneously. The partition function of any vibrational mode, therefore, is equal to:

$$z = e^{\frac{-E_{exc}}{2k_BT}} \sum_{n=0}^{\infty} e^{-n\frac{E_{exc}}{k_BT}} = \frac{e^{\frac{-E_{exc}}{2k_BT}}}{1 - e^{\frac{-E_{exc}}{k_BT}}} \tag{24}$$

The corresponding vibrational free energy is

$$F_{mode} = -k_B T\, ln(z) = \frac{1}{2}E_{exc} - ln\left(1 - exp\left(-\frac{E_{exc}}{k_B T}\right)\right) \quad (25)$$

Moreover, the corresponding vibrational energy is

$$E_{mode} = \frac{-1}{z}\left(\frac{-E_{exc}}{2}z - \frac{E_{exc}z}{1 - e^{\frac{-E_{exc}}{k_B T}}}\right) = \frac{1}{2}E_{exc} + \frac{E_{exc}}{1 - e^{\frac{-E_{exc}}{k_B T}}} \quad (26)$$

and the vibrational entropy is

$$S_{mode} = \frac{F_{mode} - E_{mode}}{T} \quad (27)$$

The total vibrational entropy S_{vib} is usually defined as the sum over all S_{mode}, except for free molecules as discussed below. Although one can similarly define E_{vib} as being the sum over all E_{mode}, it is common to simplify E_{mode} to zero-point energy E_{ZPE}, since for high E_{exc} deviation from E_{ZPE} is small, and the energy converges to $k_B T$ for E_{exc} approaching zero (the continuous limit).[55,56]

Rotational and gas-phase corrections

The final terms of the free energy as shown in Eq. 18 – rotational and translational free energy – do not apply to rotationally and translationally restricted species such as adsorbates. For non-linear free molecules, the rotational modes comprising the rotational free energy have to be calculated numerically using quantum mechanics.[57] Instead, it is common to exclude rotational energies since they originate from low-energy modes, and replace vibrational, rotational, and translational entropies by the experimentally obtained entropies in the desired phase.

All specific calculations discussed above do not take into account that the results may deviate from physical reality due to the assumptions underlying the exchange-correlation functional. Note that one of the main reasons to perform DFT calculations is to find intermediates which otherwise cannot be observed. For these intermediates, we have to reasonably assume that the energies or trends are accurate, which emphasizes the need to compare density functionals if there is any doubt. For observable species for which sufficient experimental data is available, we may compare the calculated formation energies to their experimentally obtained equivalents. Even if there is a large difference between both, we must not ignore the effect correcting these formation energies has on reaction energies between corrigible and incorrigible species. It is hence customary to apply gas-phase, or DFT, corrections ΔG_{corr} only where deviations are greater than average for the exchange-correlation functional, thereby increasing the odds of DFT errors cancelling out for the other intermediates. There are several studies which compare the DFT errors for different exchange-correlation functionals;[35,41–44] the errors listed in these works can be used to estimate the target DFT errors for one's own set of free molecules.

By including all relevant terms discussed above, we obtain the entire free energy for any system:

$$G = E_{DFT} + E_{vib} - TS + \Delta H_{phase} + \Delta G_{corr} \quad (28)$$

1.2.5. Kinetics and the nudged elastic band method

Along with the thermodynamics discussed above, chemical kinetics are relevant for our computational study of chemical reactions. Here, we define a reaction as a transition of the chemical coordinates from a set of atomic configurations centring around one local minimum to a set of configurations around another minimum. For diffusion processes, the interatomic distances of the migrating species are maintained or shifted slightly; conversely, for chemical reactions, the optimum interatomic distances between the reactant atoms (and ratios between them) are changed beyond the point they may (or may not) be considered to constitute a chemical bond. The rate of a chemical reaction, therefore, depends on the net motion of atoms from the reactant configuration space to the product configuration space.

Although it is possible to simulate reaction trajectories for individual configurations, and hence calculate the exact reaction probability at specific temperatures, it is more common to approximate the reaction rate using *transition state theory* (TST).[58,59] In TST, it is assumed that the kinetic energies on different configurations are distributed randomly and all reactions occur near the lowest energy point on the boundary between the reactant and product configurations.[59] This lowest energy point is an optimum along all possible directions, except the one perpendicular to the boundary; hence, it is also called a saddle point. The atomic configuration at this saddle point is called the *transition state* (TS). The reaction rate in the TST approximation is dependent on the thermodynamic probability of the saddle point, as expressed in the Eyring equation:[59]

$$k = \frac{\tau k_B T}{h} e^{\frac{-\Delta G^{\ddagger}}{k_B T}} \tag{29}$$

In Eq. 29, k is the reaction rate constant or the rate per amount of reactant, and τ is the transmission coefficient or probability of successfully crossing the saddle point. $\Delta G^{\ddagger}$ is the free energy difference between the reactant state and the transition state (TS), which is similar to the free energy of the initial and final modes in that:

$$G^{\ddagger} = E^{\ddagger}_{DFT} + E^{\ddagger}_{vib} - TS^{\ddagger}_{vib} \tag{30}$$

In this equation, the vibrational energies and entropies are taken along the boundary, as opposed to the entire atomic coordinate space for initial and final states. Each TS must lie on a trajectory between the local optimum of the reactant configurations and the local optimum of the product configurations. To ensure this, there are several methods to find valid transition states: one such method is the dimer method. In this method twin configurations, which differ by a deformation perpendicular towards a hypothetical boundary, move up towards the boundary and are deformed to align with the gradient towards the saddle point. Another way to find a transition state is the nudged elastic band (NEB) method, which is used in the work presented in this thesis. The NEB method involves creating several images, starting at the reactant and product configurations and deforming them towards a hypothetical transition state, along a hypothetical trajectory.[60] All images, apart from the reactant and product images, are relaxed; as opposed to the relaxation

towards the local minimum as described above, in this relaxation there are additional *spring* forces between each subsequent image to keep the images as closely together as possible:

$$\vec{F}_{NEB}(n) = \vec{F}(n) + k_{n-1,n}(\vec{r}_n - \vec{r}_{n-1}) + k_{n,n+1}(\vec{r}_{n+1} - \vec{r}_n) \quad (31)$$

with $\vec{F}$ being the force exerted by electrons and external fields, and k being individual spring constants.[60] When the images are converged, they align with the trajectory as closely as the spring constants and number of images allow. The TS configuration can be found either by sampling the atomic coordinates nearby the highest-energy image and minimising the atomic forces, or by forcing the top image n_t against the potential gradient component along the trajectory tangent $\hat{\tau}_{tan}$ in the climbing-image NEB method:[61]

$$\vec{F}_{NEB}(n_t) = \vec{F}(n_t) - 2\left(\vec{F}(n_t) \cdot \hat{\tau}_{tan}\right)\hat{\tau}_{tan} + k_{n_t-1,n_t}\left(\vec{r}_{n_t} - \vec{r}_{n_t-1}\right) + k_{n_t,n_t+1}\left(\vec{r}_{n_t+1} - \vec{r}_{n_t}\right) \quad (32)$$

Both the NEB and the climbing-image NEB method are illustrated in Fig. 1.

1.3. DFT methods for electrochemistry simulations

By applying the thermodynamic and kinetic methods described above, in the context of the theoretical discussion also described above, we can model solids and molecular systems in general. However, the complexity of heterogeneous electrochemical systems requires us to take some additional considerations into account, and other methods to be applied. A laboratory-scale heterogeneous electrocatalytic system consists of a solid electrode in contact with an electrolyte, with a counter electrode (in)directly submerged in the same electrolyte, and a bias potential and current source connecting both, as shown in Fig. 2. There are several additional aspects or interactions not described by calculation of single molecules using the methods discussed above. These include longer-range delocalisation of electrons in solids; simulation of the active surface of the catalyst; adsorbate-solvent and saddle point as a red circle. Interstitial images are shown as black circles, spring interactions

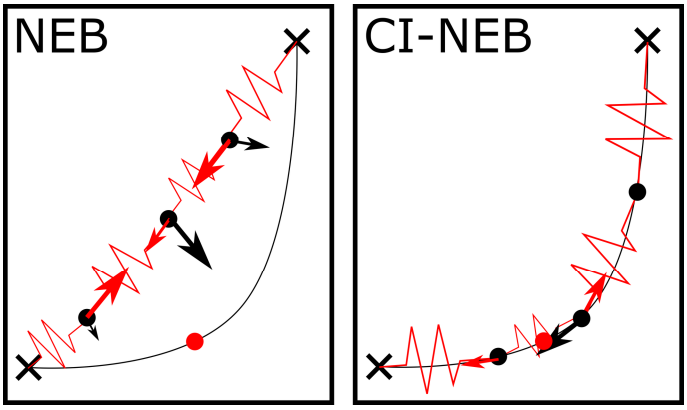

Figure 1. Comparison of NEB and climbing-image NEB methods. The reactant and product configurations are shown as crosses, the optimum trajectory between them as a black curve, and the springs, and external and spring forces using black and red arrows, respectively.

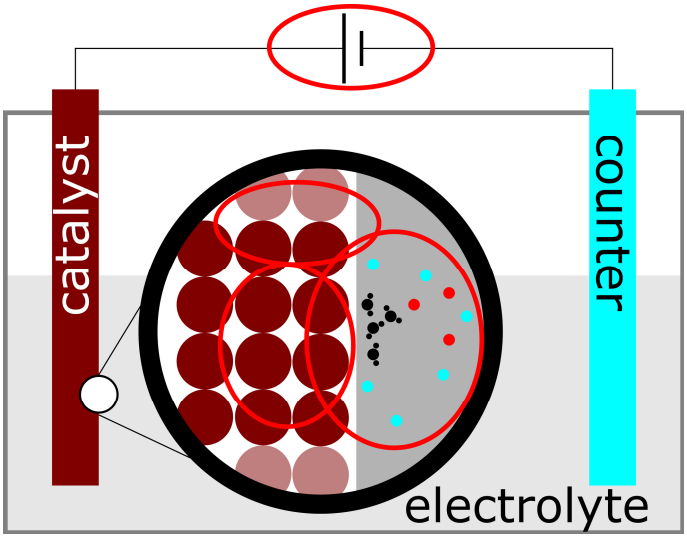

Figure 2. Simplified model of a heterogeneous electrochemical system; aspects and interactions of interest in computational models are highlighted using red ellipses.

using red adsorbate-electrolyte interactions; and applying a (simulated) electric potential to the target electrode.

1.3.1. Simulation of solids and *k*-point sampling

Simulating solids can be done by calculating the electronic Kohn-Sham orbitals in a periodic unit cell. A common way of implementing these wavefunctions is using *projector-augmented waves* (PAW). Projector-augmented waves are built up from plane waves, which are perturbed by pseudopotential wavefunctions addressed above to take care of high-density gradients in spheres surrounding individual atoms; interactions between plane waves and pseudopotential wavefunctions are taken into account separately from the interactions between plane waves.[46] If one chooses a small unit cell to calculate a solid, only a limited number of short-range electronic states is taken into account. This fails to describe many long-range electron-electron interactions and wavefunctions which define the band structure, and affects the energy of the solid and its interactions with adsorbates. Larger unit cells are unwieldy to calculate, since the calculation time scales as $O(N^3)$ with respect to the number of electrons in the system.[62] We must calculate the entire Brillouin zone of a small-cell system to improve electronic energy calculations while limiting the overall computational cost.

The Brillouin zone is the reciprocal unit cell, which means that all *k* points within the Brillouin zone other than the gamma point (Γ, $\vec{k} = \vec{0}$) correspond to wavefunctions which are periodic beyond the unit cell boundary, the so-called Bloch functions:[63]

$$u_{n,\vec{k}}(\vec{r}) = \chi_n(\vec{r})e^{i\vec{k}\cdot\vec{r}} \tag{33}$$

with χ_n being a projector augmented wave. Hence, we can add $\vec{k}$ to the PAWs building the Kohn-Sham orbitals, which are identical in terms of potential energy and density distribution yet affect the kinetic energy in Eq. 9:

$$\hat{T}u_{n,\vec{k}}(\vec{r}) = \frac{-\hbar^2}{2m}\nabla^2\varphi_{n,\vec{k}}(\vec{r})e^{i\vec{k}\cdot\vec{r}} = \frac{-\hbar^2}{2m}\left(-i\nabla + \vec{k}\right)^2\varphi_{n,\vec{k}}(\vec{r})e^{i\vec{k}\cdot\vec{r}} \quad (34)$$

Note that the shape of Kohn-Sham orbitals within the unit cell may depend on $\vec{k}$, partially because the higher-energy states within the Brillouin zone remain unoccupied. If one optimises the Kohn-Sham orbitals for all $\vec{k}$ using the combined electron density of the $\vec{k}$ combined, one obtains a more accurate density distribution.

In practice, the Brillouin zone is sampled using a limited number of points. Specifically, the Monkhorst-Pack grid is widely used: *k* points are distributed equally over the Brillouin zone, with either their point of mass lying on the Γ point or one specific *k* point at Γ.[64] By calculating the total DFT energies for the individual $\vec{k}$ as described above, and subsequently integrating over the interpolated energies between the *k* points, we can estimate the total energy of the supercell. The quality of the band structure and overall energy of the system generally improves with increasing *k* point densities, although computational costs increase simultaneously. Additionally, more important than sampling many *k* points is sampling the right *k* points, which trace the key parts of the band structure most accurately. Converging the *k* point distribution is necessary to improve energetic and physical accuracy while retaining computational efficiency.

1.3.2. The electrode-electrolyte interface and solvation

When an optimum *k* point distribution has been found for a solid, and the lattice parameters of the solid have been optimised, we can use the interatomic distances to construct a surface. Since our unit cell and corresponding calculations need to be continuous in all dimensions to properly simulate a solid surface, we have to cut the original bulk unit cell into slabs. These consist of several layers from the original bulk cell or from its supercells, which expose facets usually described by their Miller indices. The outermost layers, which are directly exposed to adsorbates, the medium or vacuum depending on the type of calculations, relax under the influence of their local environments, which means that the interatomic distances differ from those in the bulk.[65] One may choose to relax all layers, which is technically more accurate yet requires many layers for the centremost layers to behave like the underlying bulk. Conversely, one can keep the layers on one surface fixed in bulk positions, while relaxing the other layers. This method is used for slabs in the work presented in this thesis, and requires optimising the number of layers to ensure the desired reaction or formation energies converge satisfactorily.

As addressed in the context of surface relaxation, we must describe the properties of the electrode-electrolyte interface. For vacuum conditions, this is trivial, and the only consideration is to eliminate spurious (dipolar) interactions between separate periodic

slabs. However, if a medium is present, one has to take into account the stabilisation of the surface and adsorbed species by the solvent and (if present) the electrolyte. Here, we need to apply a solvation model. Solvation may be described by *implicit* solvation methods and *explicit* solvation methods. Implicit solvation describes the medium as a continuum response of the solvent to the charge densities. Generally, this response is based on the displacement of charge in the electrolyte, and the electric permittivity of the medium, which both stabilise the electric field emanating from the surface and adsorbates.[66] Explicit solvation methods involve the direct (DFT) calculation of atomic nuclei and electrons from solvent molecules. The advantage of using implicit solvation methods over explicit solvation methods is that the former do not require the calculation of various different molecule configurations, nor the electrons and nuclei inside, hence efficiently simulating bulk solvent behaviour without additional DFT costs.[67,68] However, exclusion effects caused by (Pauli) repulsion between solvent molecules and electrolyte species are ill-represented by implicit solvation models – especially when dealing with non-flat surfaces and adsorbates – and specific structurally dependent interactions such as hydrogen bonding may only be simulated properly using explicit solvent molecules.[69,70]

1.3.3. Simulating the applied electric potential

The last aspect to be taken into account in computational electrochemistry is the applied electric potential itself. The primary effect of the applied potential is that the formation energy of the intermediate is shifted with respect to the coupled reaction in the reference electrode, and a secondary effect is that charge may accumulate on the electrode, thereby affecting near-surface electric fields and the structure of the solvent at the electrode. In other terms, for a redox reaction with oxidiser A and reductor B:

$$A + ne^- \rightarrow A^{n-}; B \rightarrow B^+ + e^- \tag{35}$$

the overall reaction energy

$$\Delta G_{r,n} = \Delta G_{A,n}(U = 0) - n(\Delta G_B - eU) + \Delta\Delta G_f(U) \tag{36}$$

for redox stoichiometry n, reaction energy $\Delta G_{r,n}$, product formation energy $\Delta G_{A,n}$, counter formation energy ΔG_B, electrochemical potential U, and combined solvation energy and field effect $\Delta\Delta G_f(U)$. If water or H^+ is oxidised or reduced, the corresponding redox reaction is

$$A + nH^+ + ne^- \rightarrow AH_n; \frac{1}{2}H_2 \rightarrow H^+ + e^- \tag{37}$$

Assuming solvation or adsorbate stabilisation is independent of the applied potential, we can ignore $\Delta\Delta G_f(U)$ and calculate the onset potential with respect to the reversible hydrogen electrode:

$$U = \frac{1}{e}\left(\Delta G_{f,n} - \frac{n}{2}\Delta G_{H_2}\right) \tag{38}$$

for ΔG_{H_2} as the (reference) formation energy of $H_2(g)$. This approach to the counter-reaction is called the *computational hydrogen electrode* (CHE),[71] which was extensively used in the work presented in this thesis. The CHE method has some limitations, some of which touch

on the weaknesses in DFT. One such limitation is that surface fields and solvent structure effects caused by applied potentials are not taken into account. Another limitation is that the model does not account for intermediates with a net charge different from either reactant or product. This effectively assumes that the reaction step involves concerted proton-electron transfer, which does not necessarily apply in reality.[72]

By performing the calculations and applying (gas-phase or phase transition) corrections as listed in Section 1.2, and use the computational methods for electrochemistry discussed in Section 1.3, we can describe the entire electrochemical process from reactant to product.

1.4. Scope of this thesis

In the preceding sections of this chapter, we presented density functional theory calculations and computational methods, and discussed various considerations we need to consider regarding the efficient simulation of heterogeneous electrocatalysis. By using and building upon these methods and considerations, we studied the formation of various molecules and catalyst surfaces, and the structure of *operando* catalyst-electrolyte interfaces involved in energy storage. This research will be presented and discussed in the following chapters of this thesis.

In Chapters 2 and 3, we present two studies on carbon-based energy storage through carbon monoxide (CO) reduction. In Chapter 2, we start by describing the onset of carbon chain formation on late transition metals: the reduction of CO to C_2 species on late transition metal (100) surfaces, its reaction pathways and corresponding onset potentials.[56] Hori *et al.* found that Cu(100) shows greater rates of C_2 formation from CO than either Cu(111) or other late transition metals, and Calle-Vallejo and Koper described the most likely reduction mechanism on Cu(100) using DFT.[55] We find that both the calculated onset potentials and derived trends across the range of late transition metals point towards Cu(100) being the lowest overpotential transition metal (100) surface for ethylene production. However, for ethanol production, both onset potentials and derived trends favour Ag(100), which poses some interesting considerations for the usage of Ag in catalysts selective towards ethanol.

Chapter 3 discusses a subsequent step in carbon chain growth, namely co-reduction of CO with C_2 products created on Cu(100) to form C_3 species. There are two main mechanisms which may underlie this process: hydroformylation (alkene-CO coupling) and carbonyl-CO coupling. Hori *et al.* showed that Cu(711) surfaces produce significantly greater amounts of C_3 products than Cu(100), which indicates (111)-type steps may promote C_3 formation. Using exhaustive and granular nudged elastic band calculations, we first calculated the barriers for ethylene-CO and acetaldehyde-CO coupling reactions on Cu(100) and on Cu(711). These calculations show that acetaldehyde-CO coupling is strongly favoured on Cu compared to hydroformylation, and confirm that (111) steps further improve the coupling barrier between acetaldehyde and CO. Secondly, the onset potentials towards all C_3 products obtained through hydrogenation and dehydration lie well positive of the C_2 onset

potential. Hence, if a C_2 compound is produced on Cu(711), and it couples to CO, there is no effective thermodynamic barrier to any C_3 product.

In Chapter 4, we continue discussing the effect various surface sites have on reaction intermediates. This chapter, however, is our first foray into oxygen reduction: here we extend the work by Calle-Vallejo *et al.* on solvation of *OH on Pt with limited numbers of solvent water molecules,[73] or micro-solvation, for several late transition metals.[74] We find that there is a linear relation between the generalised coordination number of most surface sites for each metal,[75–77] as long as the nanoparticles maintain their shapes. For Ag, Au, Pd, the solvation energies are independent of the binding energy as is the case with Pt; since micro-solvation energies on Pt are close to those calculated via explicit solvation using many water molecules, it is likely that micro-solvation is accurate for the other late transition metals as well. On the other hand, solvation decreases for more strongly binding adsorption sites on Ir, which indicates that stronger binding interactions may actively modify solvation.

The final three chapters, 5 to 7, explore various aspects of fundamental electrochemistry on Pt(111): from efficient and durable hydrogen evolution reaction (HER) with graphene overlayers, through describing corrosion under highly negative potentials, to the restructuring of the surface during at increasingly high anodic potentials. In Chapter 5, we present a collaboration between experiment and theory: the properties and mechanism of hydrogen adsorption on graphene-covered Pt(111).[78] Graphene is expected to block ions in solution from disrupting the HER, and may even accelerate the reaction relative to the bare Pt surface: it is known that Pt(111) overbinds H by 0.10 eV compared to the reaction rate optimum, and graphene may interfere with Pt-H binding. Our experiments indicate that H atoms indeed bind more weakly on Pt(111) when the latter is covered by a layer of graphene; the corresponding calculations on various H coverages on bare and graphene-covered Pt(111) show a weakening of ~0.06 eV, which supports the hypothesis that HER is kinetically aided by the presence of graphene. Also, H does not permeate through graphene hexagons, yet migrates from the aqueous medium through vacancies as observed using SEM measurements. As the nature of the vacancies cannot be directly observed, we computed the diffusion kinetics for *H under graphene, and diffusion thermodynamics of H near graphene vacancies. It transpires that H can readily diffuse underneath graphene, and removing two adjacent atoms from a graphene layer provides a channel for H atoms to adsorb and move underneath the graphene bulk. These findings support the usage of (defective) graphene for more efficient and durable HER catalysis on platinum electrodes.

Chapter 6 describes what happens to the Pt(111) surface when it is left unprotected, and driven to negative potentials far beyond the HER onset. Cathodic corrosion takes place under these conditions, which means that part of the Pt surface is effectively reduced, desorbs, and forms Pt nanoparticles. Platinum hydrides are considered the main intermediate of cathodic corrosion. Therefore, it is likely that the formation of the main surface-bound cathodic corrosion intermediate involves high surface densities of hydrogen – greater than 1 monolayer (ML) H in and underneath the surface Pt layer – and complex

detachable hydride structures. To find candidate structures for high-density platinum hydrides, we adsorbed single monolayers of Pt and multiple layers of H onto a Pt(111) slab, in various configurations and stacking patterns. 2 ML H forms an island of stability across a broad range of applied potentials, relative to near-2 ML H structures containing H vacancies or additional H atoms. Moreover, successive relaxation results in a remarkably stable 3 ML H configuration at ~-0.4 V vs RHE. This structure consists of a network of highly-coordinated platinum atoms supported by a full monolayer of hydrogen, and is possibly a hydride precursor for the cathodic corrosion of Pt(111).

Finally, in Chapter 7 we discuss the restructuring of the Pt(111) surface under oxidative electrochemical conditions.[79] The usual hypothesis is that this restructuring occurs through place exchange, in which oxygen is incorporated into the surface and pushes platinum atoms outwards. Van Spronsen *et al.* observed a possible alternative cause of this pit formation: the formation of complex stripe or hexagonal spokewheel structures while exposing Pt(111) to 1 and 2.2 bar O_2, respectively, in which several Pt atoms appear to be expelled from the newly created surface structures.[80] We performed calculations on stripes consisting of PtO_2 units, with various PtO_2/Pt(surface) ratios and stripe configurations, and various on-surface O coverages. Beyond 1.2 V vs RHE, with increasingly positive applied potentials, the stripe structures with PtO_2/Pt(surface) = 6/7, 7/8, or 8/9 are most stable as opposed to on-surface O configurations; this is consistent with the SEM observations, and oxygen coverages derived from XPS measurements, by van Spronsen *et al.*[80] Moreover, the interatomic spacing in the three most stable structures is similar to literature values for bulk PtO_2. Our calculations, therefore, support the stripe formation hypothesis for surface restructuring during oxidative cycling of Pt(111).

In summary, we present in this thesis a broad range of computational simulations of heterogeneous electrocatalytic processes, focussing on reaction efficiency and the structure of the active surface. We find that for those systems for which experimental data is available in literature, our computational results correspond well to experiment. Moreover, we derive novel computational methods, and prove their applicability across a broad range of possible catalyst materials. This thesis provides a basis for further research into energy storage, whether computational or experimental, and carbon-based or hydrogen-related, and elucidates several processes and trends necessary to further the field of electrocatalysis for energy storage.

Bibliography

1 J.-Y. Lee, J. Marotzke, G. Bala, L. Cao, S. Corti, J. P. Dunne, F. Engelbrecht, E. Fischer, J. C. Fyfe, C. Jones, A. Maycock, J. Mutemi, O. Ndiaye, S. Panickal and T. Zhou, in *Climate Change 2021: The Physical Science Basis. Contribution of Working Group I to the Sixth Assessment Report of the Intergovernmental Panel on Climate Change*, eds. V. Masson-Delmotte, P. Zhai, A. Pirani, S. L. Connors, C. Péan, S. Berger, N. Caud, Y. Chen, L. Goldfarb, M. I. Gomis, M. Huang, K. Leitzell, E. Lonnoy, J. B. R. Matthews, T. K. Maycock, T. Waterfield,

O. Yelekçi, R. Yu and B. Zhou, Cambridge University Press, Cambridge, United Kingdom and New York, NY, USA, 2021, pp. 553–672.

2 IPCC, *Climate Change 2021: The Physical Science Basis. Contribution of Working Group I to the Sixth Assessment Report of the Intergovernmental Panel on Climate Change*, Cambridge University Press, Cambridge, United Kingdom and New York, NY, USA, 2021.

3 C. McGlade and P. Ekins, The geographical distribution of fossil fuels unused when limiting global warming to 2 °C, *Nature*, 2015, **517**, 187–190.

4 P. Moriarty and D. Honnery, Can renewable energy power the future?, *Energy Policy*, 2016, **93**, 3–7.

5 D. Welsby, J. Price, S. Pye and P. Ekins, Unextractable fossil fuels in a 1.5 °C world, *Nature*, 2021, **597**, 230–234.

6 Treaty Section of the Office of Legal Affairs of the United Nations, United Nations Treaty Collection, https://treaties.un.org/pages/ViewDetails.aspx?src=TREATY&mtdsg_no=XXVII-7-d&chapter=27&clang=_en, (accessed July 17, 2022).

7 United Nations Framework Convention on Climate Change, The Paris Agreement | UNFCCC, https://unfccc.int/process-and-meetings/the-paris-agreement/the-paris-agreement, (accessed July 17, 2022).

8 C. Song, Global challenges and strategies for control, conversion and utilization of CO2 for sustainable development involving energy, catalysis, adsorption and chemical processing, *Catal. Today*, 2006, **115**, 2–32.

9 N. S. Lewis and D. G. Nocera, Powering the planet: Chemical challenges in solar energy utilization, *Proc. Natl. Acad. Sci.*, 2006, **103**, 15729–15735.

10 L. Hirth, The market value of variable renewables: The effect of solar wind power variability on their relative price, *Energy Econ.*, 2013, **38**, 218–236.

11 P. Denholm and R. M. Margolis, Evaluating the limits of solar photovoltaics (PV) in traditional electric power systems, *Energy Policy*, 2007, **35**, 2852–2861.

12 K. Engeland, M. Borga, J.-D. Creutin, B. François, M.-H. Ramos and J.-P. Vidal, Space-time variability of climate variables and intermittent renewable electricity production – A review, *Renew. Sustain. Energy Rev.*, 2017, **79**, 600–617.

13 N. Kittner, F. Lill and D. M. Kammen, Energy storage deployment and innovation for the clean energy transition, *Nat. Energy*, 2017, **2**, 1–6.

14 P. J. Hall and E. J. Bain, Energy-storage technologies and electricity generation, *Energy Policy*, 2008, **36**, 4352–4355.

15 C. Budischak, D. Sewell, H. Thomson, L. Mach, D. E. Veron and W. Kempton, Cost-minimized combinations of wind power, solar power and electrochemical storage, powering the grid up to 99.9% of the time, *J. Power Sources*, 2013, **225**, 60–74.

16 A. Varone and M. Ferrari, Power to liquid and power to gas: An option for the German Energiewende, *Renew. Sustain. Energy Rev.*, 2015, **45**, 207–218.

17 S. Zhang, Q. Fan, R. Xia and T. J. Meyer, CO_2 Reduction: From Homogeneous to Heterogeneous Electrocatalysis, *Acc. Chem. Res.*, 2020, **53**, 255–264.

18 R. Francke, B. Schille and M. Roemelt, Homogeneously Catalyzed Electroreduction of Carbon Dioxide—Methods, Mechanisms, and Catalysts, *Chem. Rev.*, 2018, **118**, 4631–4701.

19 Y. Li, S. H. Chan and Q. Sun, Heterogeneous catalytic conversion of CO_2: a comprehensive theoretical review, *Nanoscale*, 2015, **7**, 8663–8683.
20 V. R. Stamenkovic, D. Strmcnik, P. P. Lopes and N. M. Markovic, Energy and fuels from electrochemical interfaces, *Nat. Mater.*, 2017, **16**, 57–69.
21 Z. W. Seh, J. Kibsgaard, C. F. Dickens, I. Chorkendorff, J. K. Nørskov and T. F. Jaramillo, Combining theory and experiment in electrocatalysis: Insights into materials design, *Science*, 2017, **355**, eaad4998.
22 N. Elgrishi, K. J. Rountree, B. D. McCarthy, E. S. Rountree, T. T. Eisenhart and J. L. Dempsey, A Practical Beginner's Guide to Cyclic Voltammetry, *J. Chem. Educ.*, 2018, **95**, 197–206.
23 T. Iwasita and F. C. Nart, In situ infrared spectroscopy at electrochemical interfaces, *Prog. Surf. Sci.*, 1997, **55**, 271–340.
24 F. Lin, Y. Liu, X. Yu, L. Cheng, A. Singer, O. G. Shpyrko, H. L. Xin, N. Tamura, C. Tian, T.-C. Weng, X.-Q. Yang, Y. S. Meng, D. Nordlund, W. Yang and M. M. Doeff, Synchrotron X-ray Analytical Techniques for Studying Materials Electrochemistry in Rechargeable Batteries, *Chem. Rev.*, 2017, **117**, 13123–13186.
25 A. A. Franco, Multiscale modelling and numerical simulation of rechargeable lithium ion batteries: concepts, methods and challenges, *RSC Adv.*, 2013, **3**, 13027–13058.
26 P. A. Kollman, I. Massova, C. Reyes, B. Kuhn, S. Huo, L. Chong, M. Lee, T. Lee, Y. Duan, W. Wang, O. Donini, P. Cieplak, J. Srinivasan, D. A. Case and T. E. Cheatham, Calculating Structures and Free Energies of Complex Molecules: Combining Molecular Mechanics and Continuum Models, *Acc. Chem. Res.*, 2000, **33**, 889–897.
27 J.-R. Hill and J. Sauer, Molecular Mechanics Potential for Silica and Zeolite Catalysts Based on ab Initio Calculations. 2. Aluminosilicates, *J. Phys. Chem.*, 1995, **99**, 9536–9550.
28 H. M. Senn and W. Thiel, QM/MM Methods for Biomolecular Systems, *Angew. Chem. Int. Ed.*, 2009, **48**, 1198–1229.
29 J. M. Boereboom, P. Fleurat-Lessard and R. E. Bulo, Explicit Solvation Matters: Performance of QM/MM Solvation Models in Nucleophilic Addition, *J. Chem. Theory Comput.*, 2018, **14**, 1841–1852.
30 G. Kresse and J. Furthmüller, Efficiency of ab-initio total energy calculations for metals and semiconductors using a plane-wave basis set, *Comput. Mater. Sci.*, 1996, **6**, 15–50.
31 W. Kohn, A. D. Becke and R. G. Parr, Density Functional Theory of Electronic Structure, *J. Phys. Chem.*, 1996, **100**, 12974–12980.
32 J. C. Slater, The Theory of Complex Spectra, *Phys. Rev.*, 1929, **34**, 1293–1322.
33 P. Hohenberg and W. Kohn, Inhomogeneous Electron Gas, *Phys. Rev.*, 1964, **136**, B864–B871.
34 W. Kohn and L. J. Sham, Self-Consistent Equations Including Exchange and Correlation Effects, *Phys. Rev.*, 1965, **140**, A1133–A1138.
35 R. Peverati and D. G. Truhlar, Quest for a universal density functional: the accuracy of density functionals across a broad spectrum of databases in chemistry and physics, *Philos. Trans. R. Soc. Math. Phys. Eng. Sci.*, 2014, **372**, 20120476.

36 C. J. Cramer and D. G. Truhlar, Density functional theory for transition metals and transition metal chemistry, *Phys. Chem. Chem. Phys.*, 2009, **11**, 10757–10816.
37 J. P. Perdew, K. Burke and M. Ernzerhof, Generalized Gradient Approximation Made Simple, *Phys. Rev. Lett.*, 1996, **77**, 3865–3868.
38 J. Klimeš, D. R. Bowler and A. Michaelides, Chemical accuracy for the van der Waals density functional, *J. Phys. Condens. Matter*, 2009, **22**, 022201.
39 J. P. Perdew, M. Ernzerhof and K. Burke, Rationale for mixing exact exchange with density functional approximations, *J. Chem. Phys.*, 1996, **105**, 9982–9985.
40 A. D. Becke, A new mixing of Hartree–Fock and local density-functional theories, *J. Chem. Phys.*, 1993, **98**, 1372–1377.
41 N. Mardirossian and M. Head-Gordon, Thirty years of density functional theory in computational chemistry: an overview and extensive assessment of 200 density functionals, *Mol. Phys.*, 2017, **115**, 2315–2372.
42 L. P. Granda-Marulanda, A. Rendón-Calle, S. Builes, F. Illas, M. T. M. Koper and F. Calle-Vallejo, A Semiempirical Method to Detect and Correct DFT-Based Gas-Phase Errors and Its Application in Electrocatalysis, *ACS Catal.*, 2020, **10**, 6900–6907.
43 R. Urrego-Ortiz, S. Builes and F. Calle-Vallejo, Fast Correction of Errors in the DFT-Calculated Energies of Gaseous Nitrogen-Containing Species, *ChemCatChem*, 2021, **13**, 2508–2516.
44 M. O. Almeida, M. J. Kolb, M. R. V. Lanza, F. Illas and F. Calle-Vallejo, Gas-Phase Errors Affect DFT-Based Electrocatalysis Models of Oxygen Reduction to Hydrogen Peroxide, *ChemElectroChem*, 2022, **9**, e202200210.
45 M. Born and R. Oppenheimer, Zur Quantentheorie der Molekeln, *Ann. Phys.*, 1927, **389**, 457–484.
46 P. E. Blöchl, Projector augmented-wave method, *Phys. Rev. B*, 1994, **50**, 17953–17979.
47 D. R. Hamann, M. Schlüter and C. Chiang, Norm-Conserving Pseudopotentials, *Phys. Rev. Lett.*, 1979, **43**, 1494–1497.
48 N. Marzari, D. Vanderbilt, A. De Vita and M. C. Payne, Thermal Contraction and Disordering of the Al(110) Surface, *Phys. Rev. Lett.*, 1999, **82**, 3296–3299.
49 J. W. Gibbs, in *Elementary Principles in Statistical Mechanics: Developed with Especial Reference to the Rational Foundation of Thermodynamics*, eds. Charles Scribner's sons and E. Arnold, University Press John Wilson and Son, Cambridge, U.S.A., 1902, pp. 32–45.
50 A. Zannoni, 1999.
51 P. A. M. Dirac and R. H. Fowler, On the theory of quantum mechanics, *Proc. R. Soc. Lond. Ser. Contain. Pap. Math. Phys. Character*, 1926, **112**, 661–677.
52 Bose, Plancks Gesetz und Lichtquantenhypothese, *Z. Für Phys.*, 1924, **26**, 178–181.
53 A. Togo and I. Tanaka, First principles phonon calculations in materials science, *Scr. Mater.*, 2015, **108**, 1–5.
54 W. Heisenberg, Über quantentheoretische Umdeutung kinematischer und mechanischer Beziehungen., *Z. Für Phys.*, 1925, **33**, 879–893.

55 F. Calle-Vallejo and M. T. M. Koper, Theoretical Considerations on the Electroreduction of CO to C2 Species on Cu(100) Electrodes, *Angew. Chem. Int. Ed.*, 2013, **52**, 7282–7285.
56 S. Hanselman, M. T. M. Koper and F. Calle-Vallejo, Computational Comparison of Late Transition Metal (100) Surfaces for the Electrocatalytic Reduction of CO to C2 Species, *ACS Energy Lett.*, 2018, **3**, 1062–1067.
57 R. Kanya and Y. Ohshima, Pendular-limit representation of energy levels and spectra of symmetric- and asymmetric-top molecules, *Phys. Rev. A*, 2004, **70**, 013403.
58 D. G. Truhlar, B. C. Garrett and S. J. Klippenstein, Current Status of Transition-State Theory, *J. Phys. Chem.*, 1996, **100**, 12771–12800.
59 H. Eyring, The Activated Complex in Chemical Reactions, *J. Chem. Phys.*, 1935, **3**, 107–115.
60 H. Jonsson, G. Mills and K. W. Jacobsen, in *Enrico Fermi Summer School proceeding*, 1997.
61 G. Henkelman, B. P. Uberuaga and H. Jónsson, A climbing image nudged elastic band method for finding saddle points and minimum energy paths, *J. Chem. Phys.*, 2000, **113**, 9901–9904.
62 N. Schuch and F. Verstraete, Computational complexity of interacting electrons and fundamental limitations of density functional theory, *Nat. Phys.*, 2009, **5**, 732–735.
63 F. Bloch, Über die Quantenmechanik der Elektronen in Kristallgittern, *Z. Für Phys.*, 1929, **52**, 555–600.
64 H. J. Monkhorst and J. D. Pack, Special points for Brillouin-zone integrations, *Phys. Rev. B*, 1976, **13**, 5188–5192.
65 M. J. S. Spencer, A. Hung, I. K. Snook and I. Yarovsky, Density functional theory study of the relaxation and energy of iron surfaces, *Surf. Sci.*, 2002, **513**, 389–398.
66 K. Mathew, V. S. C. Kolluru, S. Mula, S. N. Steinmann and R. G. Hennig, Implicit self-consistent electrolyte model in plane-wave density-functional theory, *J. Chem. Phys.*, 2019, **151**, 234101.
67 R. F. de Morais, T. Kerber, F. Calle-Vallejo, P. Sautet and D. Loffreda, Capturing Solvation Effects at a Liquid/Nanoparticle Interface by Ab Initio Molecular Dynamics: Pt201 Immersed in Water, *Small*, 2016, **12**, 5312–5319.
68 Y. Basdogan, A. M. Maldonado and J. A. Keith, Advances and challenges in modeling solvated reaction mechanisms for renewable fuels and chemicals, *WIREs Comput. Mol. Sci.*, 2020, **10**, e1446.
69 A. Rendón-Calle, S. Builes and F. Calle-Vallejo, Substantial improvement of electrocatalytic predictions by systematic assessment of solvent effects on adsorption energies, *Appl. Catal. B Environ.*, 2020, **276**, 119147.
70 Q. Zhang and A. Asthagiri, Solvation effects on DFT predictions of ORR activity on metal surfaces, *Catal. Today*, 2019, **323**, 35–43.
71 J. K. Nørskov, J. Rossmeisl, A. Logadottir, L. Lindqvist, J. R. Kitchin, T. Bligaard and H. Jónsson, Origin of the Overpotential for Oxygen Reduction at a Fuel-Cell Cathode, *J. Phys. Chem. B*, 2004, **108**, 17886–17892.

72 M. H. V. Huynh and T. J. Meyer, Proton-Coupled Electron Transfer, *Chem. Rev.*, 2007, **107**, 5004–5064.
73 F. Calle-Vallejo, R. F. de Morais, F. Illas, D. Loffreda and P. Sautet, Affordable Estimation of Solvation Contributions to the Adsorption Energies of Oxygenates on Metal Nanoparticles, *J. Phys. Chem. C*, 2019, **123**, 5578–5582.
74 S. Hanselman, F. Calle-Vallejo and M. T. M. Koper, Using micro-solvation and generalized coordination numbers to estimate the solvation energies of adsorbed hydroxyl on metal nanoparticles, *submitted*.
75 F. Calle-Vallejo, J. I. Martínez, J. M. García-Lastra, P. Sautet and D. Loffreda, Fast Prediction of Adsorption Properties for Platinum Nanocatalysts with Generalized Coordination Numbers, *Angew. Chem. Int. Ed.*, 2014, **53**, 8316–8319.
76 F. Calle-Vallejo, P. Sautet and D. Loffreda, Understanding Adsorption-Induced Effects on Platinum Nanoparticles: An Energy-Decomposition Analysis, *J. Phys. Chem. Lett.*, 2014, **5**, 3120–3124.
77 F. Calle-Vallejo and A. S. Bandarenka, Enabling Generalized Coordination Numbers to Describe Strain Effects, *ChemSusChem*, 2018, **11**, 1824–1828.
78 N. Arulmozhi, S. Hanselman, V. Tudor, X. Chen, D. van Velden, G. F. Schneider, F. Calle-Vallejo and M. T. M. Koper, Energetics and kinetics of hydrogen electrosorption on a graphene-covered Pt(111) electrode, *submitted*.
79 S. Hanselman, I. T. McCrum, M. J. Rost and M. T. M. Koper, Thermodynamics of the formation of surface PtO_2 stripes on Pt(111) in the absence of subsurface oxygen, *Phys. Chem. Chem. Phys.*, 2020, **22**, 10634–10640.
80 M. A. van Spronsen, J. W. M. Frenken and I. M. N. Groot, *Nat. Commun.*, 2017, 8.